Green Chemistry

Accepted Manuscript

ROYAL SOCIETY OF CHEMISTRY

www.rsc.org/greenchem

Graphical Abstract

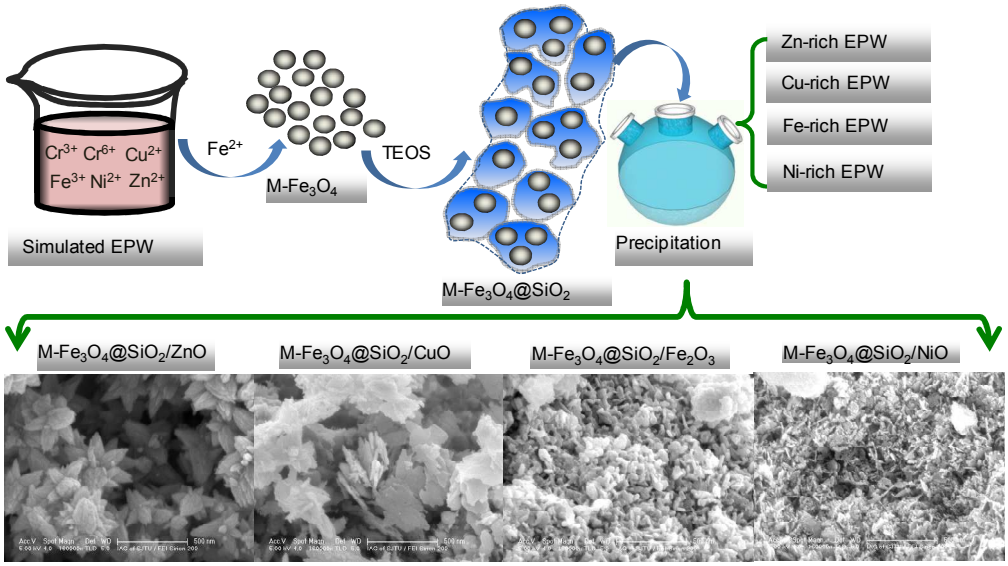

Heavy metal recovery for the fabrication of the mixed-Fe_3O_4@SiO_2/metal oxide magnetite photocatalysts from electroplating wastewater

Cite this: DOI: 10.1039/c0xx00000x

www.rsc.org/xxxxxx

ARTICLE TYPE

Heavy metal recovery from electroplating wastewater by synthesis of the mixed-Fe_3O_4@SiO_2/metal oxide magnetite photocatalysts

Shouqiang Huang, Lin Gu, Nanwen Zhu,* Kaili Feng, Haiping Yuan, Ziyang Lou,* Yiqun Li, and Aidang Shan

Received (in XXX, XXX) Xth XXXXXXXXX 20XX, Accepted Xth XXXXXXXXX 20XX
DOI: 10.1039/b000000x

Heavy metal recovery is a promising way to reduce the pollution from electroplating wastewater (EPW), and the magnetite photocatalysts of the mixed-ferrite (M-Fe_3O_4)@SiO_2/metal oxides were prepared to reuse the heavy metals from the simulated-EPW (S-EPW) and the real-EPW (R-EPW). In this work, four pure magnetite photocatalysts of M-Fe_3O_4@SiO_2/ZnO, M-Fe_3O_4@SiO_2/CuO, M-Fe_3O_4@SiO_2/Fe_2O_3, and M-Fe_3O_4@SiO_2/NiO were synthesized via a simple precipitation reaction, where the M-Fe_3O_4@SiO_2 core-shell nanoparticles were served as the magnetic cores and supports for metal oxides. The structures, morphologies, and magnetic properties of these magnetite photocatalysts were characterized, and then the photocatalytic performances of the pure and complex magnetite photocatalysts (M-Fe_3O_4@SiO_2 supported single and mixed-metal oxides) were tested and compared using the methyl orange (MO) degradation experiments. It was found that M-Fe_3O_4@SiO_2/ZnO had the best photocatalytic performance in the pure magnetite photocatalysts, with the MO removal rate of 91.5%, followed by M-Fe_3O_4@SiO_2/NiO of 37.4%, M-Fe_3O_4@SiO_2/Fe_2O_3 of 19.0%, and M-Fe_3O_4@SiO_2/CuO of 17.6%. The removal rates were 17.4% and 13.2% for the complex magnetite photocatalysts prepared from S-EPW and R-EPW, respectively. More than 98% of the heavy metals can be recovered from EPW through the synthesis of the magnetite photocatalysts simultaneously.

Introduction

Electroplating wastewater (EPW) contains various heavy metal ions, such as Cr^{6+}, Cr^{3+}, Cu^{2+}, Zn^{2+}, Fe^{3+}, and Ni^{2+}, which may be detrimental to the surround environment and human health if they are not treated in a right way. Precipitation,[1] filtration,[2] ion exchange,[3] and adsorption[4, 5] have been widely applied in the EPW treatment, while they could just use parts of heavy metals in EPW, without fully utilization of heavy metal resources. During recent years, fabrication of Fe_3O_4/ZnCr-layered double hydroxides (LDH) from Zn-rich EPW and Cr-rich EPW as absorbents,[6] and Cu@C nanowires from Cu-rich EPW as non-enzymatic glucose sensors have been reported,[7] while these studies only focus on some types of EPW, and the utilization field is also limited. "Ferrite process" is a common way for the heavy metal reused from EPW, through incorporating heavy metals into the lattice points of spinel ferrites.[8] Thus, the mixed ferrite (M-Fe_3O_4) products are generated, which can be used in many fields, such as biomedical applications, magnetic resonance imaging, nanocatalysis, and magnetic recycling.[9] However, M-Fe_3O_4 belongs to the limited solid solution, and the heavy metal fixed capacity in M-Fe_3O_4 is low. The fixed heavy metal content in M-Fe_3O_4 follows a strict proportion, and Fe source is always a limited factor. Besides the combination of heavy metals by M-Fe_3O_4, it is more interesting if the catalytic properties of these heavy metals can be improved. In EPW, there are some common metal ions, such as Zn^{2+}, Cu^{2+}, Fe^{3+}, or Ni^{2+}, which can be prepared as semiconductors for photocatalysis. Therefore, the development of ferrite photocatalysts from EPW is one of the attractive ways.

It is known that many metal oxides, which contained Zn^{2+}, Cu^{2+}, Fe^{3+}, or Ni^{2+}, show the photocatalytic abilities.[10] For examples, ZnO is a n-type and wide bandgap semiconductor with photocatalytic activity similar to that of TiO_2,[11] CuO is a common p-type and narrow bandgap semiconductor with potential application in photocatalytic hydrogen production,[12] α-Fe_2O_3 is a n-type and narrow bandgap semiconductor with aroused intensive study as an electrochemical photocatalyst,[13, 14] and NiO is a p-type and wide bandgap semiconductor with high hole mobility for efficient photocatalysis.[15] On the other hand, the separation of the nanostructured photocatalysts is a major bottleneck according to the practical experience, while magnetically recyclable has been proven to be an efficient way for separation.[9, 16, 17] Thus, M-Fe_3O_4 can be introduced in the photocatalysts as the supports to solve the separation problem. Currently, Fe_3O_4/ZnO,[18] Fe_3O_4/Fe_2O_3,[19] and Fe_3O_4/NiO[20] have been synthesized for the purpose of photocatalysis or adsorption. Nevertheless, oxidation and acid corrosion of Fe_3O_4 particles, as well as the deterioration of photocatalytic performance may occur in the Fe_3O_4/metal oxides without bonding layers.[21] SiO_2 is a promising coating material with flexibility and adhesive ability,

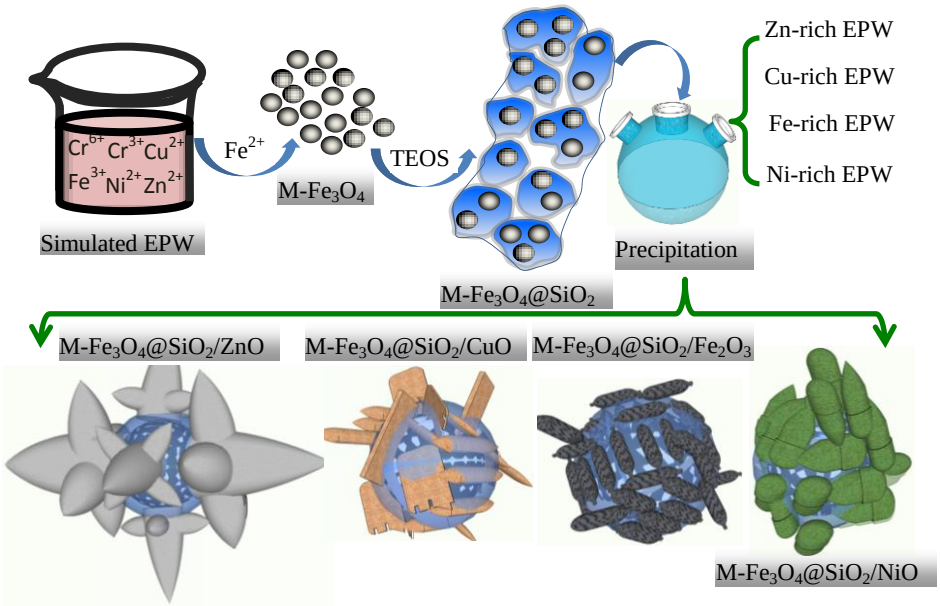

Fig. 1 Schematic illustration for the preparation of M-Fe_3O_4@SiO_2/ZnO, M-Fe_3O_4@SiO_2/CuO, M-Fe_3O_4@SiO_2/Fe_2O_3, and M-Fe_3O_4@SiO_2/NiO.

and it can not only protect the inner Fe_3O_4 cores,[22] but also improve the mechanical properties of combination between Fe_3O_4 and metal oxides.[23] Moreover, the outer shells of SiO_2 can further stabilize the heavy metals, i. e., Cr^{3+}, Cu^{2+}, Zn^{2+}, and Ni^{2+} contained in M-Fe_3O_4, and finally enhance the photocatalytic performances of the M-Fe_3O_4@SiO_2/metal oxides. It should be pointed out that very limited works have been reported on the grafting of ZnO, CuO, Fe_2O_3, and NiO on the SiO_2 coated Fe_3O_4 nanoparticles, as well as their photocatalytic performances in degradation of organic pollutants.

In this work, pure magnetite photocatalysts of M-Fe_3O_4@SiO_2/ZnO, M-Fe_3O_4@SiO_2/CuO, M-Fe_3O_4@SiO_2/Fe_2O_3, and M-Fe_3O_4@SiO_2/NiO were prepared from the simulated-EPW (S-EPW), using a simple chemical precipitation method, where the metal oxides were directly deposited on the M-Fe_3O_4@SiO_2 nanoparticles with the sodium hydroxide added. The complex magnetite photocatalysts of M-Fe_3O_4@SiO_2 supported mixed-metal oxide were also synthesized from both S-EPW and the real-EPW (R-EPW). Then, the photocatalytic abilities of the pure and complex magnetite photocatalysts were investigated and compared in the methyl orange (MO) degradation. The structures, morphologies and magnetic properties of them were also characterized simultaneously.

Experimental methods

Chemical reagents

The main chemical reagents (analytical grade) of CrO_3, $CuSO_4$ $5H_2O$, $ZnSO_4$ $7H_2O$, $NiSO_4$ $6H_2O$, $Fe_2(SO_4)_3$, $FeSO_4$ $7H_2O$, and the $Cr_2(SO_4)_3$ solution (1.35 g mL^{-1}) were provided by Sinopharm chemical Reagent Co. Ltd (China). The S-EPW consisted of 80 mg L^{-1} Cr^{6+}, 40 mg L^{-1} Cr^{3+}, 90 mg L^{-1} Cu^{2+}, 50 mg L^{-1} Zn^{2+}, 4 mg L^{-1} Ni^{2+}, and 20 mg L^{-1} Fe^{3+}, according to practical experience.[8, 24, 25] The R-EPW was kindly provided by Shanghai Hazardous Waste Management Centre (Shanghai, China), and it contained 113.36 mg L^{-1} Cr (101.27 mg L^{-1} Cr^{6+} and 12.09 mg L^{-1} Cr^{3+}), 98.04 mg L^{-1} Cu^{2+}, 60.92 mg L^{-1} Zn^{2+}, 2.59 mg L^{-1} Ni^{2+}, and 15.6 mg L^{-1} Fe^{3+} (Table S1†).

Preparation of M-Fe_3O_4@SiO_2/metal oxides

M-Fe_3O_4 and M-Fe_3O_4@SiO_2 were chosen with the $FeSO_4$ $7H_2O$: Cr^{6+} mass ratio of 50: 1, considering both the saturated magnetization (Fig. S1b† and Table S2†) and the leaching test results (Table S3†), as shown in supporting information. Total heavy metal content of Cr^{6+}, Cr^{3+}, Cu^{2+}, Zn^{2+}, Ni^{2+}, and Fe^{3+} is 284 mg L^{-1} in S-EPW, and the magnetite photocatalysts of M-Fe_3O_4@SiO_2/ZnO, M-Fe_3O_4@SiO_2/CuO, M-Fe_3O_4@SiO_2/Fe_2O_3, and M-Fe_3O_4@SiO_2/NiO were prepared individually. In a typical procedure of M-Fe_3O_4@SiO_2/ZnO, M-Fe_3O_4@SiO_2 nanoparticles were added into a three-necked flask containing 200 mL of $ZnSO_4$ $7H_2O$ aqueous solution (284 mg L^{-1}) with continuous mechanical stirring (mass ratio of ZnO: M-Fe_3O_4@SiO_2 = 20: 1), and the mixture pH was maintained at 2 by adding H_2SO_4 solution (3 mol L^{-1}) initially. The pH value was further adjusted to 10 using NaOH solution (0.3 mol L^{-1}), and then the mixture was kept at 80 ℃ for 6 h under stirring of 200 rpm. After that, precipitates obtained via separation and washing were dried in vacuum at 60 ℃ for 10 h. The photocatalyst of M-Fe_3O_4@SiO_2/ZnO was finally obtained by calcining in vacuum at 500 ℃ for 4 h. The other magnetite photocatalysts of M-Fe_3O_4@SiO_2/CuO, M-Fe_3O_4@SiO_2/Fe_2O_3, M-Fe_3O_4@SiO_2/NiO, and pure-Fe_3O_4@SiO_2/Fe_2O_3 (P-Fe_3O_4@SiO_2/Fe_2O_3) were prepared individually in the similar process (Fig. 1). M-Fe_3O_4@SiO_2 supported mixed-metal oxides prepared from S-EPW and R-EPW, which signed as M-Fe_3O_4@SiO_2/S-metal oxides and M-Fe_3O_4@SiO_2/R-metal oxides, respectively, were also followed the same procedure, after $FeSO_4$ $7H_2O$ (molar ratio of $FeSO_4$ $7H_2O$: Cr^{6+} = 3: 1) was first added into the mixture (pH

= 2) to reduce Cr^{6+} for 15 minutes.[26] Thus, the mixed-metal oxides of Cr_2O_3, ZnO, CuO, Fe_2O_3, and NiO were synthesized simultaneously with the Cr: Cu: Zn: Ni: Fe mass ratios of 118.22: 89.67: 49.46: 3.93: 277.63 in M-Fe_3O_4@SiO_2/S-metal oxides and 113.36: 98.04: 60.92: 2.59: 380.86 in M-Fe_3O_4@SiO_2/R-metal oxides (Table S1†), respectively.

Characterization

The X-ray diffraction (XRD) measurements were performed on an automated Bruker D8 Advance X-ray Polycrystaline Diffractometer with Cu Kα radiation (λ = 1.5406 Å) in the 2θ range from 10 º to 70 º. The magnetic properties of the samples were detected using Physical Property Measurement System (PPMS-9T, Quantum Design, USA). The morphologies were characterized with NoVa NanoSEM 230 field emission scanning electron microscope (FESEM) equipped with the AZTec X-Max80 energy-dispersive spectroscopy (EDS) instrument and JEM-2100F transmission electron microscope (TEM). The X-ray photoelectron spectroscopy (XPS) test was carried out by a Kratos Axis Ultra^{DLD} spectrometer with a monochromatic Al Kα source (1486.6 eV). All the reported binding energies were corrected for charging effects by the C 1s peak (284.8 eV) of adventitious carbon on the analyzed sample surface. The absorption spectra were recorded using the Lambda 750 UV-vis-NIR (Ultraviolet-visible-Near-Infrared) spectrophotometer. The Brunauer-Emmett-Teller (BET) surface areas of the samples were performed on a nitrogen adsorption apparatus (Micromeritics, ASAP 2010 M + C) by N_2 adsorption at 77 K. The metal compositions in R-EPW and the supernatants were analyzed by an inductively coupled plasma optical emission spectrometer (ICP-OES) (iCAP6300, Thermo Electron Corp.).

Photodegradation measurements

MO was used to test the photocatalytic performances of the samples under UV-vis irradiation (1000 W high-pressure mercury lamp), with 100 mg magnetite photocatalysts and MO aqueous solutions (10 mg/L, 100 mL). The mixtures were kept in the dark with mechanical stirring for 2 h to reach the adsorption-desorption equilibrium before irradiation. 3.0 mL suspensions were collected every 15 min interval and centrifuged at 12000 rpm for 10 min. After that, the absorption peak was monitored at 464 nm by UV-vis spectrophotometer (Shimadzu UV-2450 PC, Japan). In addition, 1.0 mL of the obtained MO solution was diluted 25 times for the total organic carbon (TOC) measurement by TOC-Vcpn (Shimadzu, Japan). The hydroxyl radicals (·OH) generated in the photocatalytic reactions were detected by fluorescence spectrophotometer (F-7000, Hitachi) using terephthalic acid as a probe molecule.[27]

Results and discussion

Structure analysis

The XRD patterns of M-Fe_3O_4@SiO_2 and the M-Fe_3O_4@SiO_2/metal oxides are shown in Fig. 2. The crystal phases of M-Fe_3O_4@SiO_2 consist of Fe_3O_4, $FeCr_2O_4$, $ZnFe_2O_4$, and $CuFe_2O_4$, similar to those of M-Fe_3O_4 (50: 1) (Fig. S1a†). A broad diffraction peak is also presented at about 22.5 º(Fig. S2†), and it is ascribed to the amorphous structure of SiO_2.[28] The XRD pattern of M-Fe_3O_4@SiO_2/ZnO with high crystallization degree is

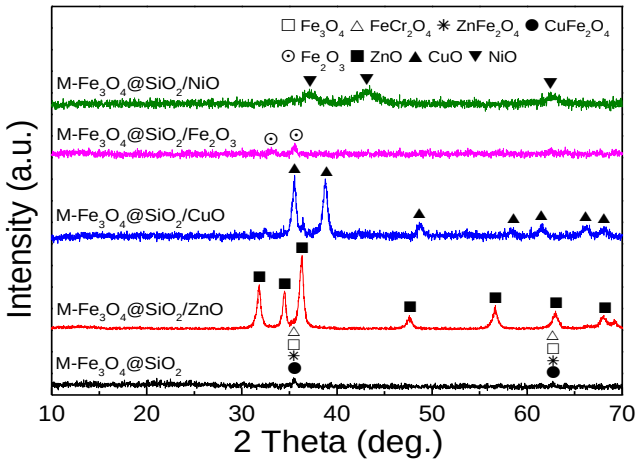

Fig. 2 XRD patterns of M-Fe_3O_4@SiO_2, M-Fe_3O_4@SiO_2/ZnO, M-Fe_3O_4@SiO_2/CuO, M-Fe_3O_4@SiO_2/Fe_2O_3, and M-Fe_3O_4@SiO_2/NiO.

attributed to the JCPDS Card No. 36-1451, and its main diffraction peaks of 31.76 º, 34.48 º, and 36.34 ºare well indexed to the (100), (002), and (101) planes of ZnO, respectively. The main diffraction peaks of M-Fe_3O_4@SiO_2/CuO are located at 35.56 º and 38.72 º, which match well with the (002) and (111) planes of CuO (JCPDS Card No. 65-2309), respectively. M-Fe_3O_4@SiO_2/Fe_2O_3 possesses broad diffraction peaks at 33.14 º and 35.64 º, which correspond to the (104) and (110) planes of Fe_2O_3 (JCPDS Card No. 33-0664), respectively. The three broad diffraction peaks of M-Fe_3O_4@SiO_2/NiO at 36.80 º, 43.06 º, and 62.36 º are in good accordance with the (111), (200), and (220) planes of NiO (JCPDS Card No. 65-2901), respectively.

Morphology analysis

The morphologies of M-Fe_3O_4@SiO_2 and the M-Fe_3O_4@SiO_2/metal oxides are observed by SEM/TEM (Fig. S3† and Fig. 3). M-Fe_3O_4@SiO_2 shows a chain-like morphology with core-shell structure, where the diameter of the M-Fe_3O_4 cores is about 15.51 nm, and the thickness of the SiO_2 shells is about 27.72 nm. A hierarchical flower-like morphology is presented in M-Fe_3O_4@SiO_2/ZnO (Fig. 3a), with the multiple petal structure assembled by nanoparticles (15 nm) (Fig. 3b), and accompanied with microporous property (3.37 nm) (Fig. 3c and Table S4†). The high-resolution TEM (HRTEM) image provides the lattice fringe spacing of 0.282 nm (Fig. 3d), which matches well with the (100) planes of ZnO, and the corresponding selected-area electron diffraction (SAED) pattern reveals the polycrystalline nature. Fig. 3e shows the nanoplate-like morphology of M-Fe_3O_4@SiO_2/CuO, with the thickness of 13 nm and the length of 200 nm (Fig. 3f and g), and the lattice fringe spacing of 0.233 nm represents the (111) planes of CuO (Fig. 3h). M-Fe_3O_4@SiO_2/Fe_2O_3 exhibits the nanorod shape, and its length and width are estimated to be 97 and 14 nm, respectively (Fig. 3i). The HRTEM image (Fig. 3k) shows a single crystal with the lattice fringe spacing of 0.252 nm ((110) planes of Fe_2O_3), and several single crystals are connected to form the nanorod particle (Fig. 3j). The length and width of M-Fe_3O_4@SiO_2/NiO with needle-plate-like morphology are about 10 and 2 nm, respectively (Fig. 3l, m, and n), and the lattice fringe spacing of 0.208 nm

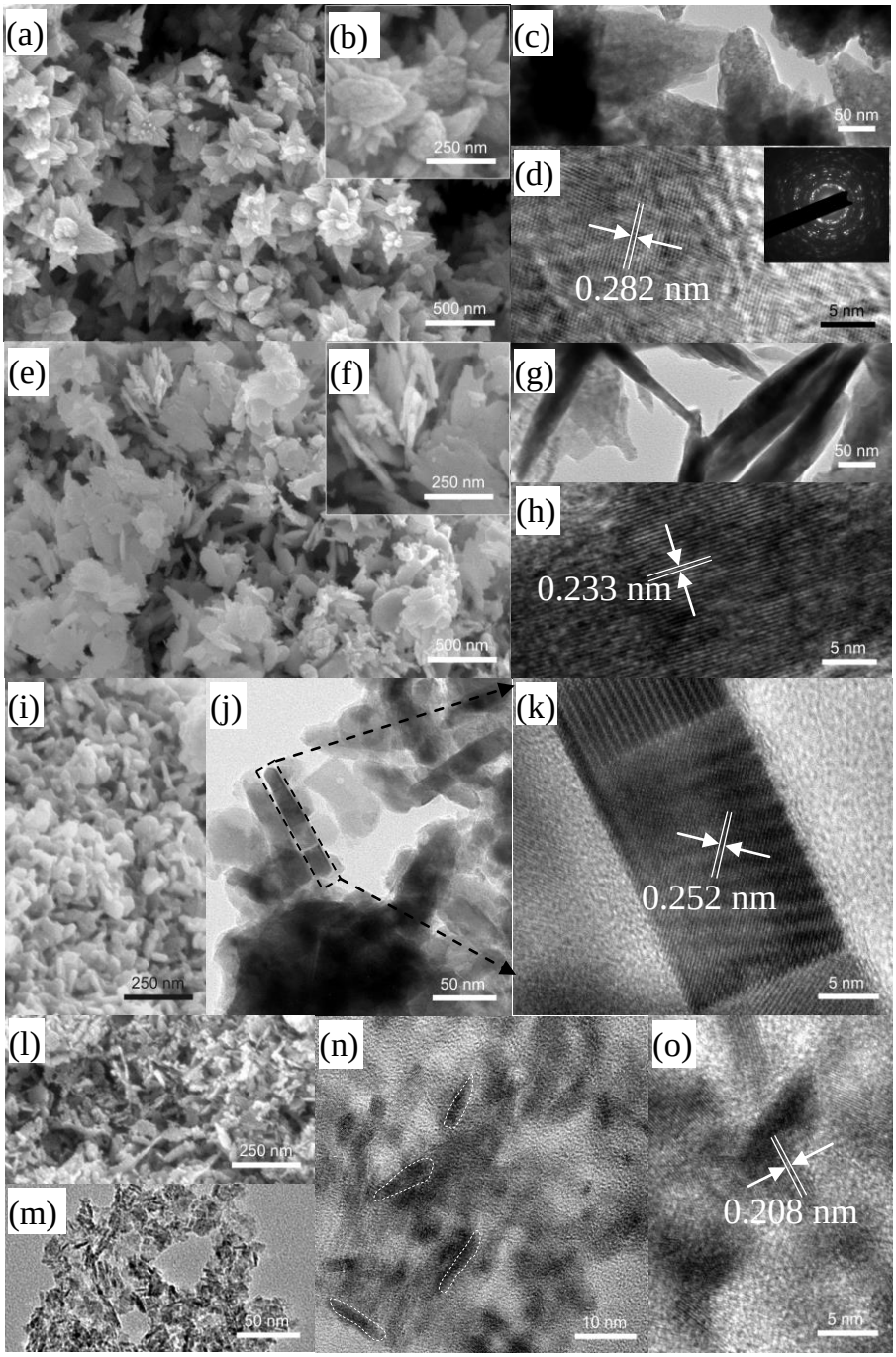

Fig. 3 (a, b) SEM, (c) TEM, and (d) HRTEM images (inset: selected-area electron diffraction (SAED) pattern) of M-Fe_3O_4@SiO_2/ZnO. (e, f) SEM, TEM (g), and (h) HRTEM images of M-Fe_3O_4@SiO_2/CuO. (i) SEM, (j) TEM, and (k) HRTEM images of M-Fe_3O_4@SiO_2/Fe_2O_3. (l) SEM, (m) TEM, and (n, o) HRTEM of M-Fe_3O_4@SiO_2/NiO.

meets the (200) planes of NiO (Fig. 3o). According to the TEM images (Fig. 3g, j, and m) of the M-Fe_3O_4@SiO_2/metal oxides, most of the metal oxides are firmly embedded in the SiO_2 layers (Fig. S3†), which is the guarantee of stability in the photocatalytic processes.

Magnetic analysis

The field dependence of magnetization curves of M-Fe_3O_4@SiO_2 and the M-Fe_3O_4@SiO_2/metal oxides measured at 300 K are shown in Fig. 4a, and the corresponding magnetic parameters are shown in Table S5†. The saturated magnetization (M_s) of M-Fe_3O_4@SiO_2 is 17.91 emu g^{-1}, lower than that (55.05 emu g^{-1}) of M-Fe_3O_4 (Fig. S1b† and Table S2†), and it is resulted from the decreased total mass of M-Fe_3O_4 in M-Fe_3O_4@SiO_2 substituted by the SiO_2 coatings. After the incorporation of ZnO and CuO, the M_s values further decreased to 0.30 and 0.49 emu g^{-1} for M-Fe_3O_4@SiO_2/ZnO and M-Fe_3O_4@SiO_2/CuO, respectively, which are mainly due to the low mass fraction of M-Fe_3O_4@SiO_2 occupied in the photocatalysts (mass ratio of ZnO or CuO:

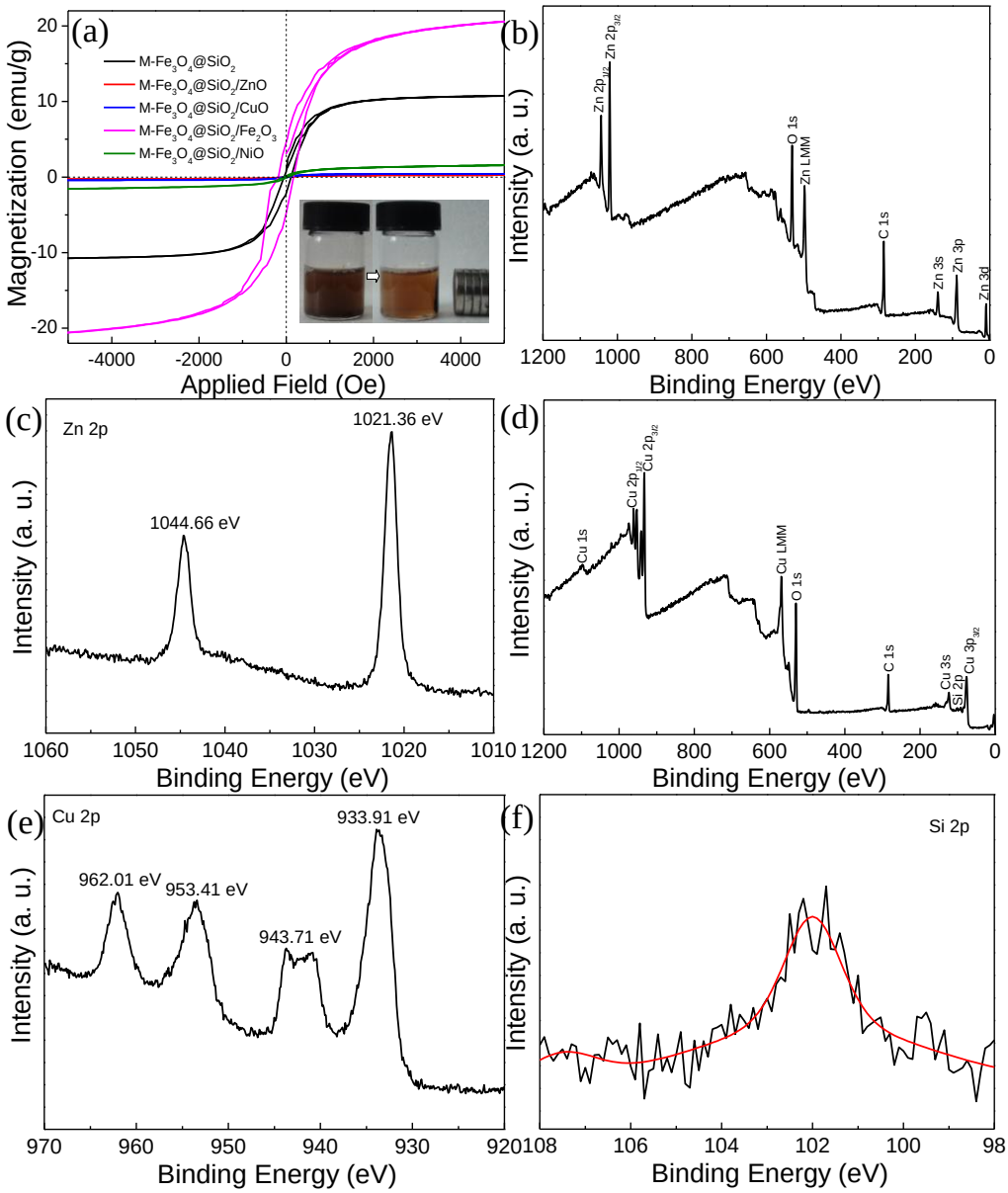

Fig. 4 (a) Room temperature (300 K) magnetic hysteresis loops of M-Fe_3O_4@SiO_2 and the M-Fe_3O_4@SiO_2/metal oxides, and the inset shows the magnetic separation of M-Fe_3O_4@SiO_2/Fe_2O_3 from their aqueous solution. XPS spectra of M-Fe_3O_4@SiO_2/ZnO: (b) survey scan, and (c) Zn 2p. XPS spectra of M-Fe_3O_4@SiO_2/CuO: (d) survey scan, (e) Cu 2p, and (f) Si 2p.

M-Fe_3O_4@SiO_2 is 20: 1). The M_s value at room temperature is supposed to reduce sharply as the particle size decreases.[29] The average particle size of ZnO is smaller than that of CuO (Fig. 3), resulting in a lower M_s value for M-Fe_3O_4@SiO_2/ZnO compared to that of M-Fe_3O_4@SiO_2/CuO. Variation of surface anisotropy will also affect M_s through changing the moment of inner M-Fe_3O_4.[30] Meanwhile, M-Fe_3O_4@SiO_2/Fe_2O_3 exhibits the highest M_s value (23.03 emu g^{-1}) (Table S5†), and even stronger than that of M-Fe_3O_4@SiO_2, since Fe is the ferromagnetic element, as well as the Ni element. Thus, M-Fe_3O_4@SiO_2/NiO also possesses higher M_s (2.28 emu g^{-1}) value compared to those of M-Fe_3O_4@SiO_2/ZnO and M-Fe_3O_4@SiO_2/CuO.

Based on the magnetic results of the four M-Fe_3O_4@SiO_2/metal oxides, the lowest M_s of M-Fe_3O_4@SiO_2/ZnO is also related to its architectural morphology. Although the EDS analysis of M-Fe_3O_4@SiO_2/ZnO demonstrates the existence of Si element (Table S6†), no M-Fe_3O_4@SiO_2 can be observed clearly in Fig. S4a†. From the XPS spectrum of M-Fe_3O_4@SiO_2/ZnO (Fig. 4b), no Si peak is presented, while the detected high-resolution spectrum of Zn 2p (Fig. 4c) exhibits well resolved doublet peaks of 1021.36 eV (Zn $2p_{3/2}$) and 1044.66 eV (Zn $2p_{1/2}$),[31] meaning that the M-Fe_3O_4@SiO_2 cores are fully wrapped by the ZnO nanoparticles. For M-Fe_3O_4@SiO_2/CuO, M-Fe_3O_4@SiO_2 is apparently appeared in the TEM image of Fig. S4b†, and it is consistent with its XPS spectrum (Fig. 4d). The binding energy of Cu $2p_{3/2}$ is located at 933.91 eV with a shake-up satellite of 943.71 eV, and the Cu $2p_{1/2}$ is observed at 953.41 with a satellite of 962.01 eV (Fig. 4e).[32] The Si 2p peak is located

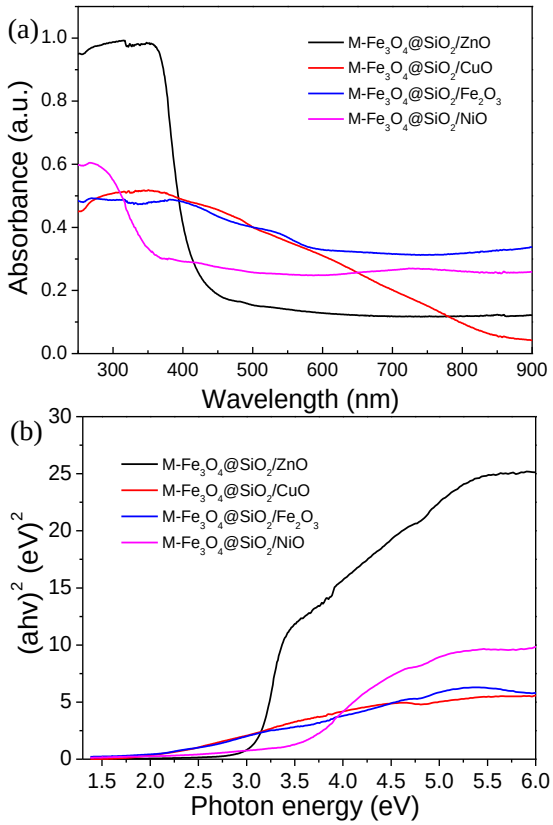

Fig. 5 (a) UV-vis-NIR diffuse reflectance spectra and (b) the plots of the $(\alpha h\nu)^2$ versus photon energy ($h\nu$) for M-Fe_3O_4@SiO_2/ZnO, M-Fe_3O_4@SiO_2/CuO, M-Fe_3O_4@SiO_2/Fe_2O_3, and M-Fe_3O_4@SiO_2/NiO.

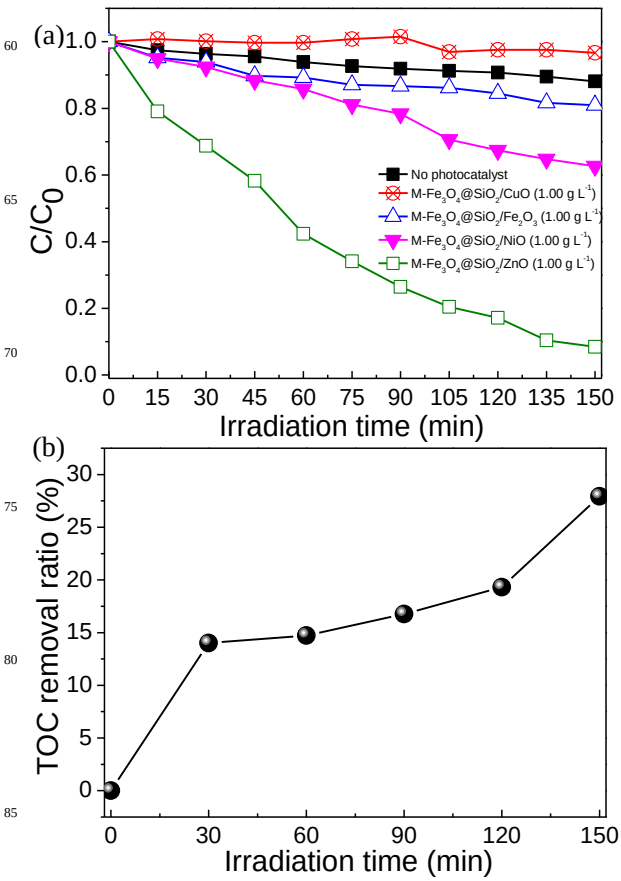

Fig. 6 (a) Photocatalytic degradations of MO for M-Fe_3O_4@SiO_2/ZnO, M-Fe_3O_4@SiO_2/CuO, M-Fe_3O_4@SiO_2/Fe_2O_3, and M-Fe_3O_4@SiO_2/NiO under UV-vis irradiation. (b) TOC removal rates of MO for M-Fe_3O_4@SiO_2/ZnO under UV-vis irradiation.

at about 102.10 eV (Fig. 4f), and the calculated mass ratio of Cu^{2+}: Si^{4+} is 46.24%: 4.01% (Table S6†). According to the above results, the dense ZnO layers on the surfaces of M-Fe_3O_4@SiO_2 lead to the lower M_s for M-Fe_3O_4@SiO_2/ZnO compared to that of M-Fe_3O_4@SiO_2/CuO. In addition, all the M-Fe_3O_4@SiO_2/metal oxides display the weak ferromagnetic property owing to their coercivity (H_c) values (> 30 Oe) (Table S5†), whereas they can be easily separated by applying a magnetic field from the treated wastewater, i. e., the magnetic separation of M-Fe_3O_4@SiO_2/Fe_2O_3 from its aqueous solution, as shown in the inset of Fig. 4a.

UV-vis-NIR absorption properties

Optical properties of the M-Fe_3O_4@SiO_2/metal oxides are measured by UV-vis-NIR diffuse reflectance spectra, as shown in Fig. 5a. M-Fe_3O_4@SiO_2/ZnO shows the strongest absorption intensity in the UV region (250-370 nm), while M-Fe_3O_4@SiO_2/NiO possesses a little higher absorption band in 250-300 nm, compared to M-Fe_3O_4@SiO_2/CuO and M-Fe_3O_4@SiO_2/Fe_2O_3. The band gap energies of the M-Fe_3O_4@SiO_2/metal oxides (Fig. 5b) can be calculated from the equation: $(\alpha h\nu)^2 \propto h\nu - E_g$, where α, h, ν, and E_g are the absorption coefficient, Plank's constant, frequency, and band gap energy (eV), respectively.[33] The absorption edge wavelengths of M-Fe_3O_4@SiO_2/ZnO and M-Fe_3O_4@SiO_2/NiO are about 393.65 and 351.27 nm, and the corresponding band gap energies are 3.15 and 3.53 eV (Table S4†), respectively, suggesting that only the UV light can be used for photocatalysis. Meanwhile, the absorption edges of M-Fe_3O_4@SiO_2/CuO and M-Fe_3O_4@SiO_2/Fe_2O_3 are extended to 610.84 (2.03 eV) and 590.48 nm (2.10 eV), which show their visible-light responding photocatalytic ability.

Photocatalytic performances

The degradation of MO aqueous solution was used to test and compare the photocatalytic performances of the M-Fe_3O_4@SiO_2/metal oxides under UV-vis light irradiation. Fig. 6a shows the MO photodegradation rates over the M-Fe_3O_4@SiO_2/metal oxides with the mass concentration of 1.00 g L^{-1}. The absorption bands of MO at 464 nm decrease gradually as the irradiation time extended for M-Fe_3O_4@SiO_2/ZnO (Fig. S5a†) and M-Fe_3O_4@SiO_2/NiO (Fig. S5b†). The highest degradation rate of 91.5% is found in the case of M-Fe_3O_4@SiO_2/ZnO after 150 min, since M-Fe_3O_4@SiO_2/ZnO shows the best light absorption property in the UV band (Fig. 5a) and the efficient electron-hole pair separation performance.[34] Under UV light irradiation, the electrons from the valence band (VB) of ZnO can be excited to the conduction band (CB), and therefore the holes (h^+) and electrons (e^-) will be generated on the VB and CB, respectively. Then, OH can be produced greatly via the reaction between holes (h^+) and H_2O in MO solutions, which can destroy

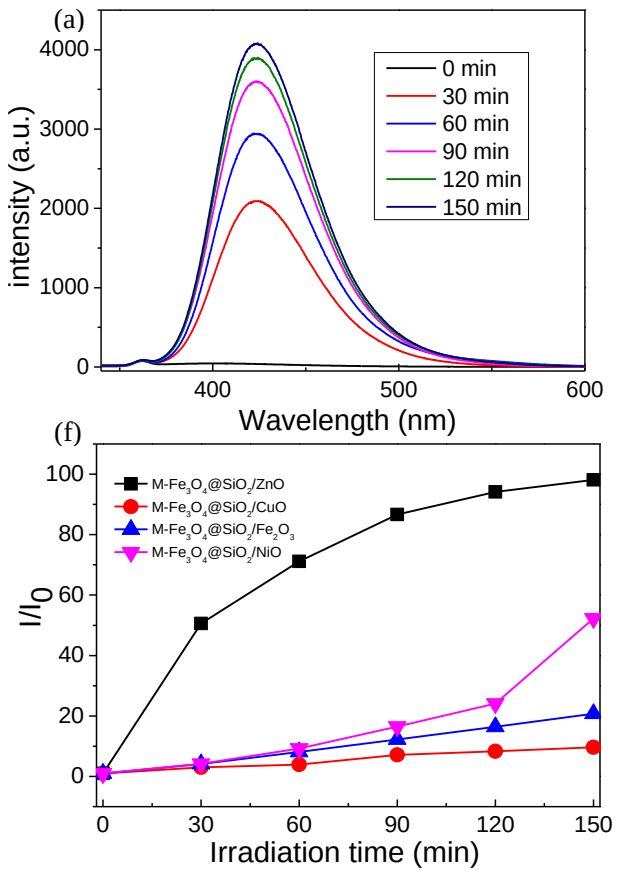

Fig. 7 (a) Time-dependent fluorescence spectra of the terephthalic acid solution (4×10^{-4} M, excitation at 321 nm) containing 20 mg of M-Fe_3O_4@SiO_2/ZnO under UV-vis light irradiation, (b) Fluorescence intensity of the emission peak at 420 nm as a function of the UV-vis irradiation time.

the MO molecules. As shown in Fig. 7a, the photoluminescence intensities of 2-hydroxyterephthalic acid at about 420 nm are enhanced gradually, indicating the increased ·OH concentration as the irradiation time extended. The highest ·OH content is exhibited over M-Fe_3O_4@SiO_2/ZnO, compared to those of other M-Fe_3O_4@SiO_2/metal oxides (Fig. 7b), which results in the best photocatalytic performance, with a TOC removal rate of 27.9% (Fig. 6b).

For other photocatalysts, M-Fe_3O_4@SiO_2/NiO shows a little higher MO degradation rate (37.4%) than those of M-Fe_3O_4@SiO_2/Fe_2O_3 (19.0%) and M-Fe_3O_4@SiO_2/CuO (3.4%) (Table S7†), because M-Fe_3O_4@SiO_2/NiO has higher light absorption intensity in the UV band (250-300 nm) (Fig. 5a) and stronger ·OH generation ability (Fig. 7b), compared to M-Fe_3O_4@SiO_2/Fe_2O_3 and M-Fe_3O_4@SiO_2/CuO. Higher BET specific surface area of M-Fe_3O_4@SiO_2/NiO is another reason, with the value of 176 m^2 g^{-1}, while only 18 and 16 m^2 g^{-1} are found in M-Fe_3O_4@SiO_2/CuO and M-Fe_3O_4@SiO_2/Fe_2O_3, respectively (Table S4†).

It should be noted that the MO degradation rate is only 3.4%, with 1.00 g L^{-1} M-Fe_3O_4@SiO_2/CuO added, and even lower than that of the self-degradation rate (11.9%) of MO. In contrast, the better degradation performance of 17.6% is obtained with 0.5 g L^{-1} M-Fe_3O_4@SiO_2/CuO added (Fig. 8a). It is reasonable to point out that the introduction of too much photocatalyst will decrease the light penetration and increase the light scattering in the quartz reactor.[35] The similar performance is also observed in the M-Fe_3O_4@SiO_2/Fe_2O_3 system, and the MO degradation rates of 16.7%, 19.4%, and 5.4% are found with the M-Fe_3O_4@SiO_2/Fe_2O_3 dosages of 0.25, 0.50, and 2.00 g L^{-1} (Fig. 8b), respectively. The optimal mass concentration will provide a large amount of active sites in the total surface area of M-Fe_3O_4@SiO_2/Fe_2O_3, which are helpful for the ·OH generation.[36]

In the M-Fe_3O_4@SiO_2/metal oxides, the magnetic cores of M-Fe_3O_4 contain the elements of Cr, Cu, Zn, and Ni. To evaluate the effects of M-Fe_3O_4 and pure Fe_3O_4 (P-Fe_3O_4) cores on the photocatalytic performances, P-Fe_3O_4@SiO_2/Fe_2O_3 is also fabricated. The MO degradation rate of 16.6% is obtained over P-Fe_3O_4@SiO_2/Fe_2O_3 (Fig. 8c and Table S7†), slightly lower than that of M-Fe_3O_4@SiO_2/Fe_2O_3 (19.0%). Thus, M-Fe_3O_4 can also be one of the potential support candidates for the magnetite photocatalyst fabrication.

Usually, EPW mainly contains the elements of Cr, Cu, Zn, Ni, and Fe, and thus the M-Fe_3O_4@SiO_2/mixed-metal oxides (Cr_2O_3, ZnO, CuO, Fe_2O_3, and NiO) will be synthesized easily from EPW. To test the photocatalytic performances of the complex magnetite photocatalysts, M-Fe_3O_4@SiO_2/R-metal oxides are fabricated, and M-Fe_3O_4@SiO_2/S-metal oxides are chosen as the control group to compare here (Fig. 8d), with the corresponding MO degradation rates of 13.2% and 17.4%, respectively. From Table S1†, the heavy metal recovery rates of Cr, Cu, Zn, Ni, and Fe in S-EPW and R-EPW are all more than 98% through the magnetite photocatalyst fabrication. Accordingly, Zn is the most critical element for the photocatalytic performances of the magnetite phtocatalysts, as shown in Fig. 6. The mass ratio of Zn: Fe in R-metal oxides is about 60.92: 380.86, lower than that of S-metal oxides (Zn: Fe = 49.46: 277.63), leading to a little lower degradation rate for M-Fe_3O_4@SiO_2/R-metal oxides, compared to that of M-Fe_3O_4@SiO_2/S-metal oxides.

The stabilities of the M-Fe_3O_4@SiO_2/metal oxides are evaluated using the cyclic experiments, and the photocatalytic performances of M-Fe_3O_4@SiO_2/ZnO, M-Fe_3O_4@SiO_2/CuO, M-Fe_3O_4@SiO_2/ZnO, and M-Fe_3O_4@SiO_2/Fe_2O_3 under UV-vis light irradiation are shown in Fig. S6†. No obvious degradation variation can be observed from the M-Fe_3O_4@SiO_2/metal oxide samples after three cycles, indicating their good stability property. Among the magnetite photocatalysts, M-Fe_3O_4@SiO_2/ZnO exhibits the best photocatalytic performance (91.5%), which is closed to that (95.4%) of the commercial Degussa P25 titania (Fig. S7†). In many cases, ZnO exhibits better photocatalytic activities compared to TiO_2 and P25.[37, 38] The lower degradation rate here is mainly owing to the reduced total amount of ZnO occupied by M-Fe_3O_4@SiO_2 in M-Fe_3O_4@SiO_2/ZnO, while the decreased BET specific surface area (15 m^2 g^{-1}) of M-Fe_3O_4@SiO_2/ZnO is another reason compared to that (50 m^2 g^{-1}) of P25. However, P25 nanoparticles in the treated wastewater are unable to reuse by the magnetic recovery method, and thus a certain advantage is displayed with the magnetite photocatalysts of the M-Fe_3O_4@SiO_2/metal oxides. The synthesis of the M-Fe_3O_4@SiO_2/metal oxides provides a potential and high-value way for the full utilization of heavy metals from EPW. The

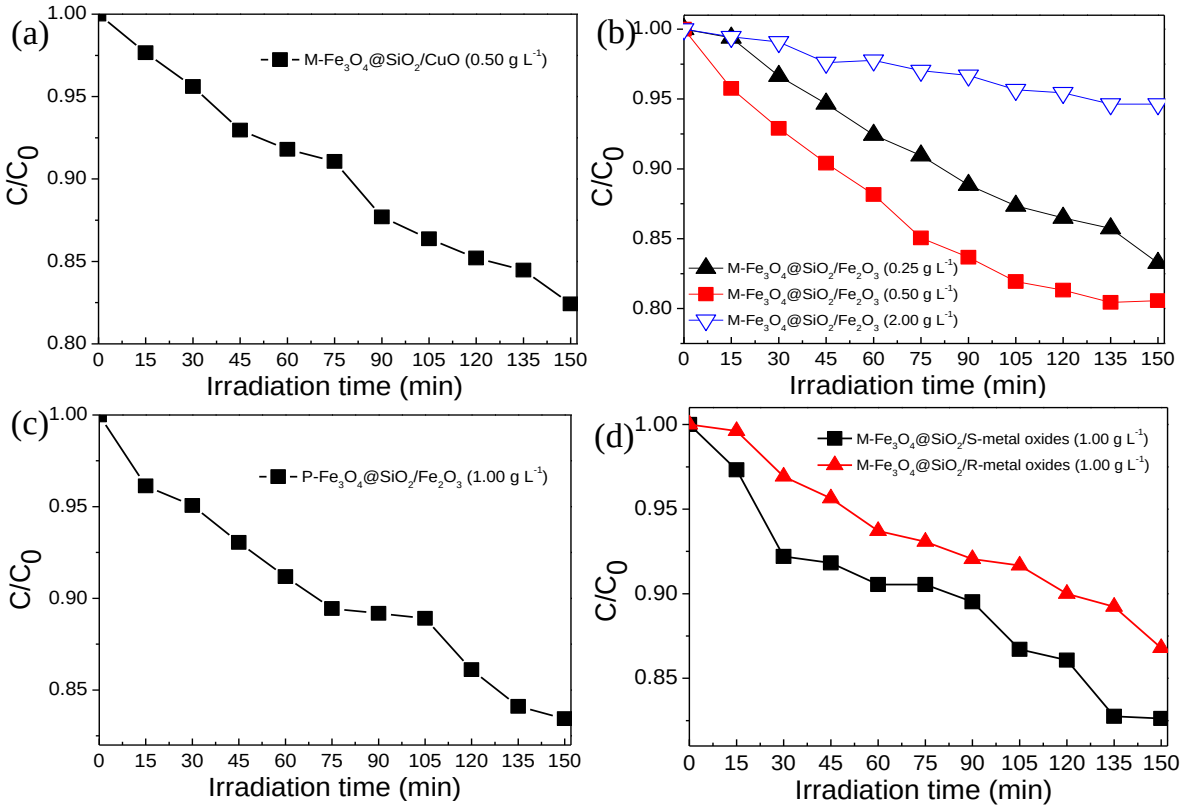

Fig. 8 Photocatalytic degradations of MO for (a) M-Fe_3O_4@SiO_2/CuO, (b) M-Fe_3O_4@SiO_2/Fe_2O_3, (c) P-Fe_3O_4@SiO_2/Fe_2O_3, and (d) M-Fe_3O_4@SiO_2/S-metal oxides and M-Fe_3O_4@SiO_2/R-metal oxides under UV-vis irradiation.

improvement of photocatalytic performances of the M-Fe_3O_4@SiO_2/metal oxides should be also implemented in the next step.

Conclusions

A novel resource utilization of EPW has been developed to prepare the magnetite photocatalysts of M-Fe_3O_4@SiO_2/metal oxides for photocatalysis. According to the types of heavy metal ions and their mass concentrations in S-EPW, M-Fe_3O_4@SiO_2/ZnO, M-Fe_3O_4@SiO_2/CuO, M-Fe_3O_4@SiO_2/Fe_2O_3, and M-Fe_3O_4@SiO_2/NiO were prepared. The structures and morphologies of the samples are related to their magnetic properties and photocatalytic performances. M-Fe_3O_4@SiO_2/ZnO has the best MO degradation rate of 91.50% in 150 min. M-Fe_3O_4@SiO_2/NiO also exhibits higher degradation rate (37.36%) than those of M-Fe_3O_4@SiO_2/Fe_2O_3 (19.02%) and M-Fe_3O_4@SiO_2/CuO (17.58%), since it possesses higher light absorption intensity in the UV band and stronger OH generation ability, as well as the higher BET specific surface area of 177 m^2 g^{-1}, compared to those of M-Fe_3O_4@SiO_2/CuO (18 m^2 g^{-1}) and M-Fe_3O_4@SiO_2/Fe_2O_3 (16 m^2 g^{-1}). For the complex magnetite photocatalysts prepared from S-EPW and R-EPW, degradation rates of 17.4% and 13.2% are attributed to M-Fe_3O_4@SiO_2/S-metal oxides and M-Fe_3O_4@SiO_2/R-metal oxides, respectively. All the M-Fe_3O_4@SiO_2/metal oxide samples have photocatalytic performance in degradation of MO, and they can be separated by an external magnetic field from the treated wastewater, suggesting that the preparation of photocatalysts from EPW is a promising method for the resource utilization of EPW.

Acknowledgments

This work was supported by National Natural Science Foundation of China (No. 41173108), "Chenguang" project by Shanghai Municipal Education Commission and Shanghai Education Development Foundation (No. Z1126862), SMC-"Chenxing" project by Shanghai Jiaotong University (2011), Key project of Science and Technology Commission of Shanghai Municipality (No. 12231202101), and Key Project of the National Research Program of China (2014BAL02B03).

Notes and references

School of Environmental Science and Engineering, Shanghai Jiao Tong University, 800 Dongchuan Rd., Shanghai, 200240, P. R.China. Fax: +86 21 34203710; Tel: +86 21 54743710; E-mail: nwzhu@sjtu.edu.cn; louworld12@sjtu.edu.cn

† Electronic Supplementary Information (ESI) available: Additional tables and figures as mentioned in the text. See DOI: 10.1039/b000000x/

1 M. Balakrishnan, V. S. Batra, J. S. J. Hargreaves and I. D. Pulford, *Green Chem.*, 2011, **13**, 16.
2 L. Alvarado, I. Rodr ́guez Torres and A. C. Chen, *Sep. Purif. Technol.*, 2013, **105**, 55.
3 Y. Q. Xing, X. M. Chen and D. H. Wang, *Environ. Sci. Technol.*, 2007, **41**, 1439.
4 I. Ali, *Chem. Rev.*, 2012, **112**, 5073.
5 B. Wang, H. Wu, L. Yu, R. Xu, T. Lim and X. W. Lou, *Adv. Mater.*, 2012, **24**, 1111
6 D. Chen, Y. Li, J. Zhang, W. H. Li, J. Z. Zhou, L. Shao and G. R. Qian, *J. Hazard. Mater.*, 2012, **243**, 152.

7 Y. X. Zhao, Z. Y. He and Z. F. Yan, *Analyst*, 2013, **138**, 559.
8 D. Chen, J. Hou, L. H. Yao, H. M. Jin, G. R. Qian and Z. P. Xu, *Sep. Purif. Technol.*, 2010, **75**, 210.
9 M. B. Gawande, P. S. Branco and R. S. Varma, *Chem. Soc. Rev.*, 2013, **42**, 3371.
10 H. Tong, S. X. Ouyang, Y. P. Bi, N. Umezawa, M. Oshikiri and J. H. Ye, *Adv. Mater.*, 2012, **24**, 229.
11 Y. Li, W. Xie, X. Hu, G. Shen, X. Zhou, Y. Xiang, X. Zhao and P. Fang, *Langmuir*, 2010, **26**, 591.
12 D. Barreca, P. Fornasiero, A. Gasparotto, V. Gombac, C. Maccato, T. Montini and E. Tondello, *ChemSusChem*, 2009, **2**, 230.
13 A. M. Balu, D. Dallinger, D. Obermayer, J. M. Campelo, A. A. Romero, D. Carmona, F. Balas, J. Santamaria, K. Yohida, P. L. Gai, C. Vargas, C. O. Kappe and R. Luque, *Green Chem.*, 2012, **14**, 393.
14 G. Wang, Y. Ling, D. A. Wheeler, K. E. N. George, K. Horsley, C. Heske, J. Z. Zhang and Y. Li, *Nano Lett.*, 2011, **11**, 3503.
15 X. F. Song and L. Gao, *J. Phys. Chem. C*, 2008, **112**, 15299.
16 M. B. Gawande, P. S. Branco, I. D. Nogueira, C. A. A. Ghumman, N. Bundaleski, A. Santos, O. M. N. D. Teodoro and R. Luque. *Green Chem.*, 2013, **15**, 682.
17 R. Chalasani and S. Vasudevan, *ACS Nano*, 2013, **7**, 4093.
18 W. Y. Chen and Y. C. Chen, *Anal. Bioanal. Chem.*, 2010, **398**, 2049.
19 X. Wei, T. F. Xie, L. L. Peng, W. Fu, J. S. Chen, Q. Gao, G. Y. Hong and D. J. Wang, *J. Phys. Chem. C*, 2011, **115**, 8637.
20 S. W. Zhang, J. X. Li, T. Wen, J. Z. Xu and X. K. Wang, *RSC Adv.*, 2013, **3**, 2754.
21 V. Belessi, D. Lambropoulou, I. Konstantinou, R. Zboril, J. Tucek,D. Jancik, T. Albanis and D. Petridis, *Appl. Catal. B: Environ.*, 2009, **87**, 181.
22 A. L. Morel, S. I. Nikitenko, K. Gionnet, A. Wattiaux, J. Lai-Kee-Him, C. Labrugere, B. Chevalier, G. Deleris, C. Petibois, A. Brisson and M. Simonoff, *ACS Nano*, 2008, **2**, 847.
23 V. Polshettiwar, R. Luque, A. Fihri, H. Zhu, M. Bouhrara, J. M. Basset, *Chem. Rev.*, 2011, **111**, 3036.
24 J. Yang, J. Peng, K. C. Liu, R. Guo, D. L. Xu and J. P. Jia, *J. Hazard. Mater.*, 2007, **143**, 379.
25 D. Park, Y. S. Yun, J. H. Jo and J. M. Park, *Ind. Eng. Chem. Res.*, 2006, **45**, 5059.
26 M. Erdem, F. Tumen, *J. Hazard. Mater.*, 2004, **109**, 71.
27 L. Q. Ye, J. Y. Liu, Z. Jiang, T. Y. Peng and L. Zan, *Nanoscale*, 2013, **5**, 9391.
28 X. G. Yu, Y. Shan, G. C. Li and K. Z. Chen, *J. Mater. Chem.*, 2011, **21**, 8104.
29 H. M. Lu, W. T. Zheng and Q. Jiang, *J. Phys. D: Appl. Phys.*, 2007, **40**, 320.
30 W. Wu, S. F. Zhang, X. H. Xiao, J. Zhou, F. Ren, L. L. Sun and C. Z. Jiang, *ACS Appl. Mater. Interfaces*, 2012, **4**, 3602.
31 M. Y. Wang, L. Sun, J. H. Cai, P. Huang, Y. F. Su and C. J. Lin, *J. Mater. Chem. A*, 2013, **1**, 12082.
32 M. Dar, S. Nam, Y. Kim and W. J. Kim, *J. Solid State Electrochem.*, 2010, **14**, 1719.
33 S. Q. Huang, L. Gu, C. Miao, Z. Y. Lou, N. W. Zhu, H. P. Yuan and A. D. Shan, *J. Mater. Chem. A*, 2013, **1**, 7874.
34 A. Mclaren, T. Valdes-Solis, G. Li and S. C. Tsang, *J. Am. Chem. Soc.*, 2009, **131**, 12540.
35 M. G. Antoniou, A. A. de la Cruz and D. D. Dionysiou, *Environ. Sci. Technol.*, 2010, **44**, 7238.
36 R. C. Wang, D. J. Ren, S. Q. Xia, Y. L. Zhang and J. F. Zhao, *J. Hazard. Mater.*, 2009, **169**, 926.
37 C. A. K. Gouvêa, F. Wypych, S. G. Moraes, N. Durán, N. Nagata and P. P. Zamora, *Chemosphere*, 2000, **40**, 433.
38 S. O. Fatin., H. N. Lim, W. T. Tan and N. M. Huang, *Int. J. Electrochem. Sci.*, 2012, **7**, 9074.